

Interferometric Calculations of Solar Radius

Max Lee *

Lab Partners: Basil Kyriacou, Connor McWard , James Mang

Department of Astronomy, University of California, Berkeley

Abstract

Interferometry provides a useful tool in accurate distance calculations over a range of scientific fields, spanning geology and astrophysics. Here we use the geometric foundations of interferometry applied to radio astronomy and compute detailed distance measurements of both our antenna setup as well as the solar radius. We find that we are able to compute the orientation of our baseline in both the east-west and north-south directions allowing accurate estimates of the solar radius. We conclude that based off of our observations, this value is $6.763 \times 10^{8+2.872 \times 10^7 m}_{-2.611 \times 10^7 m}$. We compare these results with the most recent estimates and provide insight into future works to further decrease the extent of our error.

1 Introduction

Accuracy in observational astronomy often comes down to size. The larger a telescope, the more accurate a measurement can be made. Interferometry mitigates the cost of building massive telescopes by utilizing many smaller dishes, that synthesize a large telescope. The larger the separation between the telescopes, the larger the synthesized diameter, and the more accurate of an observation can be made.

From continental drift measurements to observations of the largest objects in our universe, interferometry and its sensitivity play a key role. In the recent work of The Event Horizon Telescope [Event Horizon Telescope Collaboration, 2019] interferometry was utilized for the first ever image of a black holes event horizon, and there are current projects utilizing similar methods to better understand the history of the universe and the phenomenon that lie within.

In this work, we use a 2 antenna radio interferometer and provide an investigation into the geometric foundation of interferometry by focusing on solar measurements. Through this investigation we consider how interferometers can provide precise location synchronization for our observing orientation. We use these considerations to estimate the exact orientation of our antenna locations and the baseline length therein. We use the estimated baseline lengths to further deduce the angular radius of the sun.

In the following section we review basic interferometric theory and discuss the key equations to our work, we then discuss our antenna setup and calibration in section 2. This is followed by our presen-

tation of observational results in section 3 followed by our methods of data analysis in section 4. We use this analysis of section 4 to discuss our results in section 5 where we compare our results to previously determined values and consider possible sources of error in our measurements. We conclude in section 6 with a summary of our work and ideas for future optimization of our experiment.

1.1 Interferometric Theory

An interferometer utilizes the path length difference measured in time between two antennas and the convolution of their signals. As a source transits across the sky, the time delay between the antennas changes and can be thought of as a projection of the baseline in the direction of the source. As the antennas follow the source, the delay increases and decreases in a sinusoidal pattern known as the point source fringe rate, or $F(h_s)$ where h_s is the hour angle, defined as $h_s = lst - \alpha$ (Local Sidereal Time - Right ascension). We define this point source fringe rate for a monochromatic source as the multiplication of the sources electric field with a phase delay or,

$$F(h_s) = E(\nu, t)E(\nu, t + \tau) \quad (1)$$

where τ represents a time delay caused both geometrically and internally from cables ($\tau_g + \tau_c$). Using the wave nature of electric fields and utilizing the geometry of the interferometric setup, this can be expressed as,

$$F(h_s) = A \cos(2\pi\nu\tau'_g) + B \sin(2\pi\nu\tau'_g) \quad (2)$$

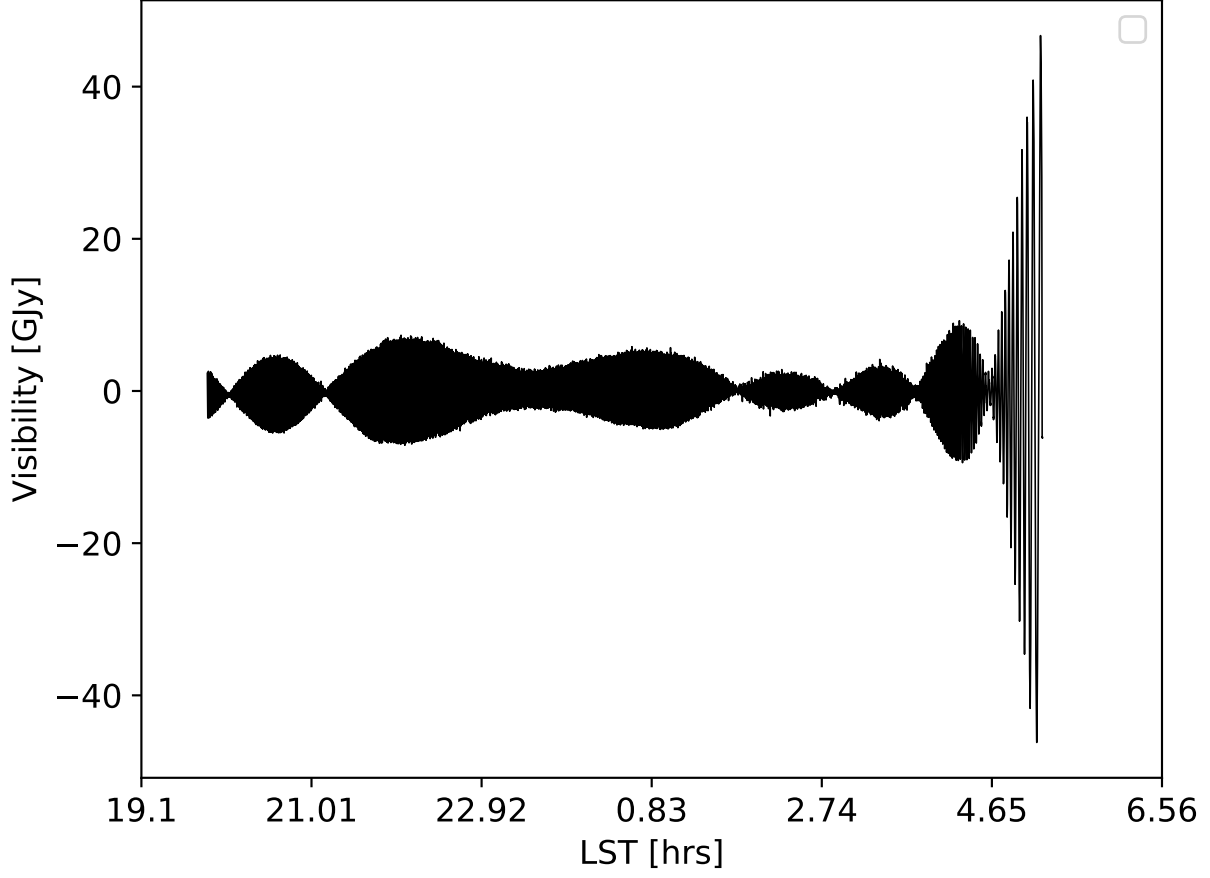


Figure 1: Using a 10.7 GHz , 2 antenna interferometer, we measure track and measure the visibility of the sun over the course of $\sim 19.84 - 5.22\text{ LST}$ on 2458924 JD . We calibrate the visibility axis using the known spectral intensity of 3C144 at 496 Jy . We see that there is a non 0 offset from arising from power introduced by the first amplifier and filter. Further we see a unique shape with both fast oscillations and enveloping oscillations.

Where

$$\begin{aligned} A &= np.\sin(2\pi\nu\tau'_c) \\ B &= np.\cos(2\pi\nu\tau'_c) \\ \nu\tau'_g &= \frac{B_{EW}}{\lambda} \cos \delta \sin h_s \end{aligned} \quad (3)$$

Where A and B are nuisance parameters representing the cable delay and parallel geometric delay of the interferometer, τ'_g is the geometric delay and is a function of hour angle, h_s , and depends upon the baseline orientation in the east west directions, B_{EW} , B_{NS} , as well as the wavelength of the interferometer, λ , and the source declination.

Intuitively, equation 2 is stating that at the horizon, the time delay between the antennas is the largest, at zenith it is the smallest. When we track a source on the sky, we are watching it traverse the

peaks and troughs of this fringe pattern.

Because our focus is not on a point source, but the sun which is a disk in the sky, we must include a modulating factor from the fourier transform of the sources shape. We can write the full visibility equation including the modulating function as,

$$R(h_s) = F(h_s)MF(h_s) \quad (4)$$

Where $MF(h_s)$ is the modulation function and in the flat sky approximation, is the Fourier transform of the source intensity. We will discuss in section 3, our hypothesis for what this function will be and use our estimates of the solar angular radius to verify our approximation in section 5.

2 Instrumentation

We begin with a description of the interferometer we used, located at Campbell Hall ($37^{\circ}52'14.1''$, $-122^{\circ}15'15.25''$, 120.0 m). We detail the signal chain used for observations highlighting the sources of errors in our instrumentation and ways in which these could be mitigated in the future. We then discuss our process of calibrating the interferometer.

2.1 Observation Setup

We use a 2 antenna interferometer with originally unknown baseline separation operating at $\sim 10.7\text{ GHz}$ and a $\sim 3^{\circ}$ beam aperture. The antenna are controllable so that they can be programmed to follow a source in the sky from an altitude of $\sim 5^{\circ}$ to $\sim 175^{\circ}$.

We make two observations, one of the sun on 2458924 *JD* from 19.84 *hrs* to 5.22 *hrs* Local Sidereal Time (LST) (See fig 1). Through this time, the sun rises from an altitude and azimuth of 23.35° , 112.24° to 5.26° , 263.83° .

Our second observation is of 3C144, The Crab Nebula ($\alpha = 5^{\text{h}}34^{\text{m}}31.95^{\text{s}}$ $\delta = 22^{\circ}52.1''$) on 2458938 *JD* from 3.24 *hrs* to 12.35 *hrs* LST. For this source we see it precess from an altitude and azimuth of 55.82° , 107.44° to 5.036° , 294.11° .

Through the observations of 3C144, we encountered several errors in the later part of the observations. One antenna stopped responding from 7.14 – 7.33 *LST* and 8.92 – 10.36 *LST*. Further, we found a large discrepancy in our data where the signal became massive between 11.6348 – 12.3127 *LST*, which we believe was due to interference with the Eastern antenna. Because of the precarious location of our telescope, in-between buildings and hills, we could also attribute the

2.2 Calibration

Our primary interest is with the solar data, so we use only a small portion of the 3C144 data for the purposes of calibration. The use of the crab nebula as a calibration source is because it is an unresolved source, with a cataloged visibility. This implies that it is distant and small enough for our beam of $\sim 3^{\circ}$ to encompass the total emission, and this value is well known.

We focus on a section of consistent data, between 5.72 – 6.49 *LST* and use this data to calibrate as seen in figure 2. We first remove power introduced at 0 frequency by a filter in the signal chain, this centers

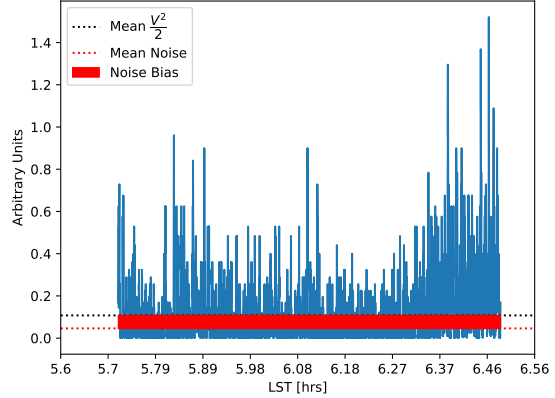


Figure 2: We take a sub-section of observations from The Crab Nebula and of the cold sky with no bright sources to determine the noise bias (*red shaded*). With this value and the mean value of $V^2/2$ (*black dotted*), we are able to calculate a constant calibration factor for our antennas.

our data at 0 which more accurately represents the true signal.

The magnitude of the visibility is represented by the peak-amplitude of the point source fringe rate. To extrapolate this out, we find the mean value of the absolute value squared of our fluctuations. Because there is noise in our data as well, the mean squared value of the data will be slightly higher than reality. To mitigate this fact, we use observations of the sky with no bright sources, only noise, to find what the noise bias or offset of our intensity. To calibrate, we then use a normalization such that,

$$\frac{\langle V_{obs} \rangle}{\sqrt{2}} + n = 496\text{ Jy} \quad (5)$$

Where V_{obs} is the observed visibility in arbitrary units, n is the noise bias and 496 *Jy* is the known value of 31C44's visibility at 10.7 *GHz*.

Figure 2 shows the squared observations of the crab nebula, as well as the calculated noise bias from observing the cold sky. We find that the scaling factor to calibrate future observations becomes, $6.51 \times 10^{12}\text{ Jy}$.

3 Results

Our observations of the sun can be in figure 1 spanning the full day. There are two explicitly interesting features we see from the shape of our data. First, that there are two oscillatory patterns occurring, a fast oscillation and an envelope. Second, the latter

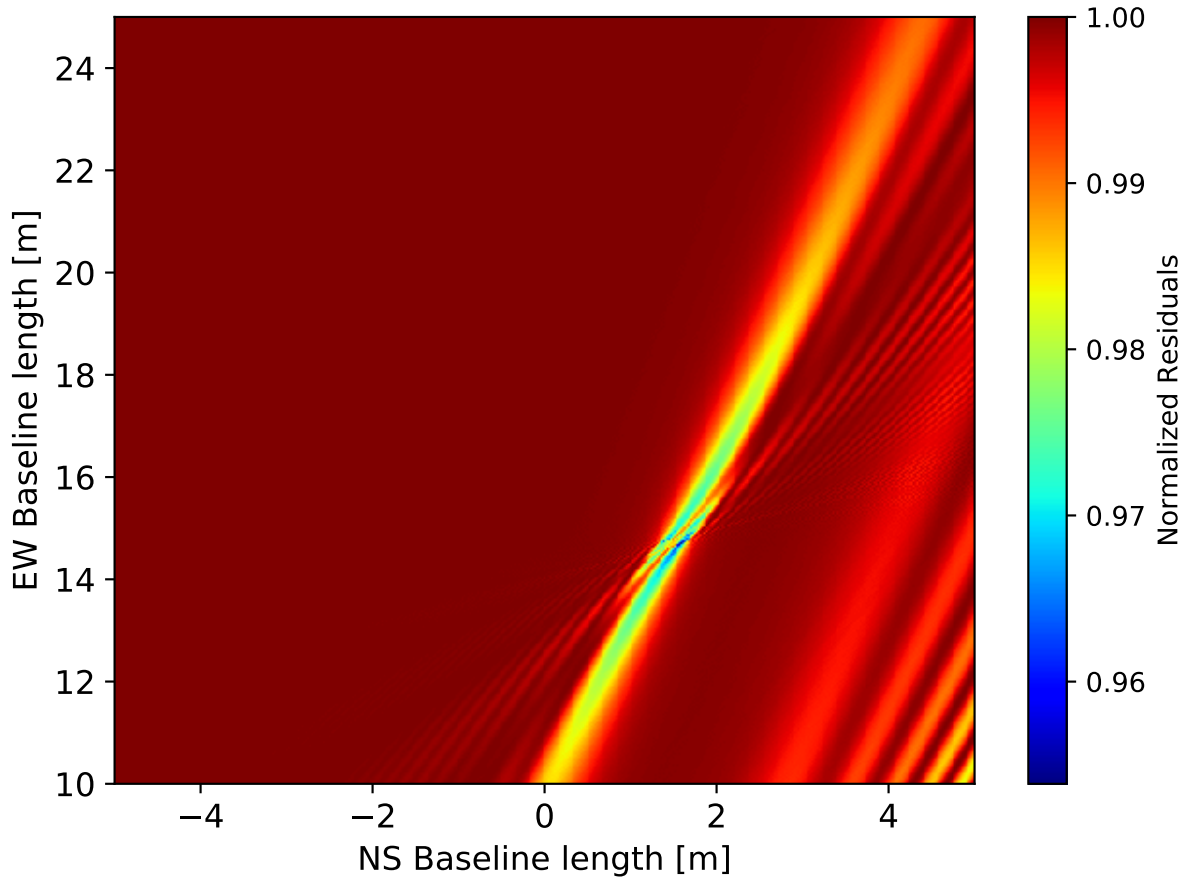


Figure 3: By guessing a range of baseline length combinations in the EW and NS directions, we perform a brute force, non-linear least squares solution to equation 2. The residuals from this analysis is plotted above, and the point where it is minimized (most blue), represents the most accurate estimation of the true baseline orientation.

part of the day sees visibility's ~ 5 times higher than that at noon. The latter feature can be explained by the fact that as the sun is setting and when it is rising, are the only points in time when the Sun is an unresolved source where we are capturing the entire flux inside of our beam. The rest of the day, we are focused on small segments of the sun's disk, providing us with a lower visibility.

The oscillatory motion of the data represents the point source fringe rate, and the modulating function of the source. The fringe rate of the point source is determined by the geometric delay occurring between the antennas, and explains why we see the tail of our data at $\sim 4.65 LST$ gradually decreasing in frequency, whereas the center at $\sim 0 LST$ has a high frequency. In section 4 we will show that we are able to isolate the point source fringe rate with accurate knowledge of the baseline orientations.

The modulating function exists because we are not viewing the sun as an unresolved source. For the most part, we are capturing a portion of the sun's disk as it traverses through the sky.

The modulating function then is the Fourier transform of the Sun's shape, and we hypothesize that because the two dimensional projection of the sun is approximately a disk, the modulating function (MF) will represent its Fourier transform, an Airy disk defined as,

$$MF = A \frac{J_1(x + \phi)}{x + \phi} \quad (6)$$

Where A is a normalization factor, x is some argument which is dependant on the hour angle ($HA = LST - RA$), ϕ is a phase, and J_1 is a Bessel Function of the first kind. We will see in section 4, that knowledge of where this function is equal to 0, provides us

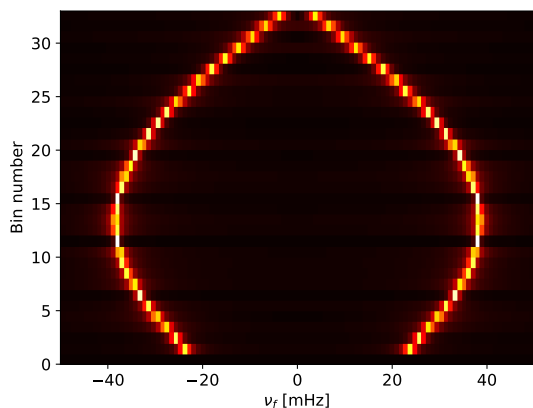


Figure 4: We put modeled solar point source fringe rate into 33 bins and Fourier transform them to find the fringe frequency of the point source, irrespective of the modulating function. The bins are connected to time, so we see that as the day progresses, the fringe frequency increases to a peak and then slows to near 0 at sunset.

with a way to estimate the solar angular radius and diameter.

To remove noise, we filter the data by Fourier transforming it, and removing the lowest and highest Fourier modes which are representative of noise rather than signal.

4 Analysis

We now discuss the process in which we analyzed the results to obtain values for key features of the interferometric observation. The visibility that we obtain is a not just a representation of the source we are observing, but also an accurate representation of the features of the antennas themselves. We outline the process of obtaining key features representing the interferometer and the sun.

4.1 Baseline location

We compute the baseline orientation using a least squares analysis on equation 2. Because the equation is non-linear with h_s residing in \cos and \sin terms, we solve it using a brute force method, where we supply a range of guesses for what the right orientation is and determine the most accurate guess by finding the minimized sum of the residuals.

We define a range of baselines around where we estimate them to reside: for $B_{EW} = [10, 25]$, for $B_{NS} = [-5, 5]$. We then use these values along with

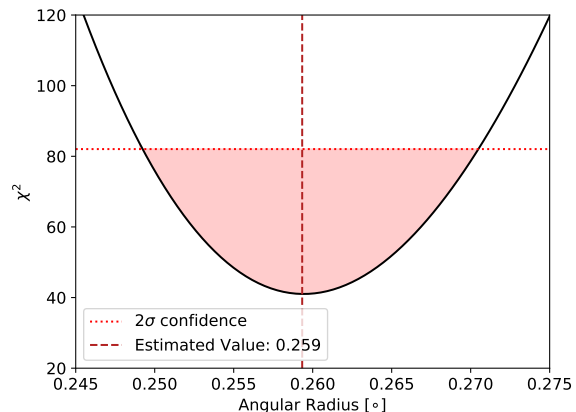


Figure 5: By comparing the known nulls of an Airy Disk, and the nulls found in the data, we perform a χ^2 analysis and find that the minimum value of χ^2 occurs at an angular radius of $.26^\circ$. We highlight the 2σ error region in red to emphasize that that our estimate spreads a range of $\sim .02^\circ$.

an estimated solar declination and right ascension to compute the least squares solution for A and B along with their residuals for every possible combination of B_{EW} and B_{NS} .

One thing to note is that the right ascension and declination of the sun vary even over the course of a day. We estimate them by calculating the mean value of the suns right ascension and declination over the course of 2458924 JD and use the mean values for the least squares solution.

Through the least squares solution, we are able solve for estimates of the constants A, B in equation 2, and the baselines. Figure 3 shows the result of the residuals for each of the baseline combinations, the smallest of which is the most accurate guess of the baseline orientation. We see that this is located at $B_{EW} = 14.68 m$, $B_{NS} = 1.59 m$.

We can now find what the point source fringe rate of the sun is, which is how the fringe would oscillate if it were a point source without a modulating function. Figure 4, shows the Fourier transform of the point source fringe rate, or local fringe frequency, binned in ~ 20 minute increments. This highlights how the sun moves through changing fringe rates projected on the sky. It grows in frequency becoming faster as the source moves to zenith and then slows its frequency as it precesses to the horizon. If we were to have captured the sun from the moment of its rising, we would expect to see a perfect symmetry in the shape about its maximum fringe frequency.

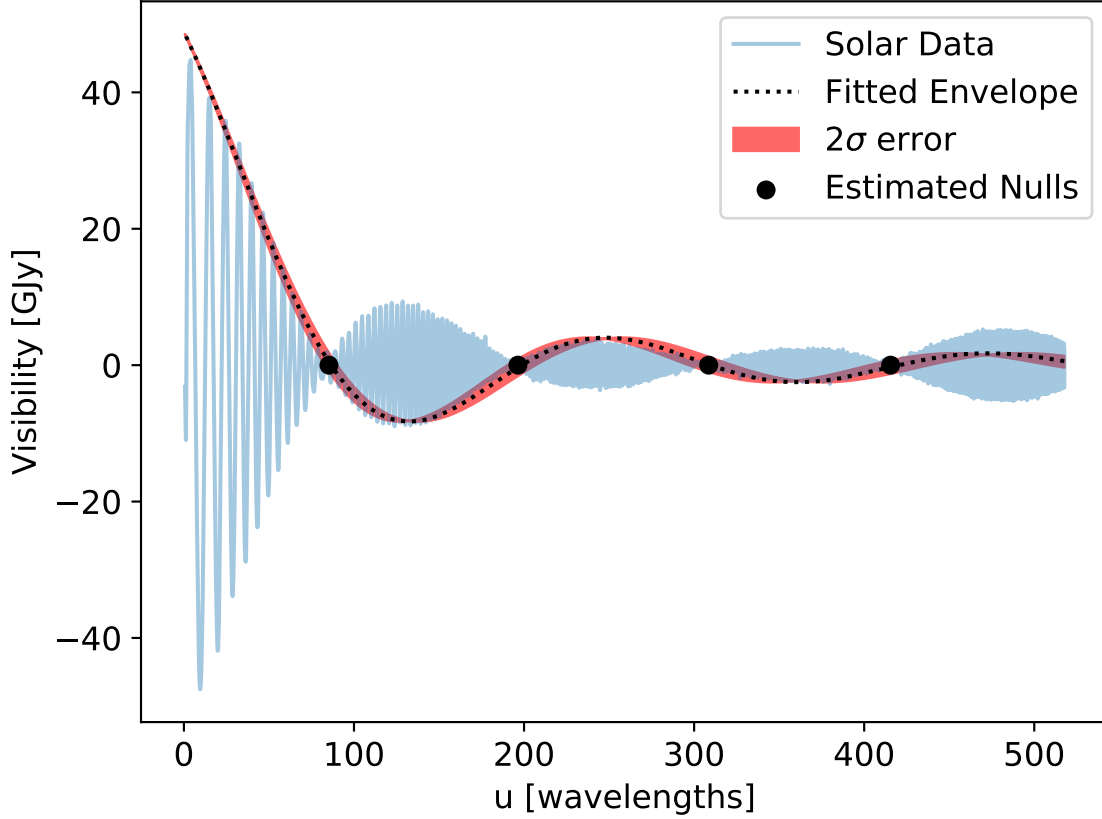


Figure 6: We perform a χ^2 minimization on the nulls of our data and the expected nulls of an Airy Disk. The minimized value provides us with an estimate for the angular radius of the sun, and 2σ error bars which we use to model the enveloping function of half of the suns data. We find that our estimate strongly agrees with the data, but seems to fail at a proper estimation at large projected baseline lengths, near 0 *LST*.

4.2 Radial Calculation

We expect the modulating function of the sun to be an airy disk as described in equation 6. With this in mind, we estimate the nulls in the modulating function of our data as a function of the projected EW baseline length, u . We define this projection as

$$u = \frac{B_{EW}}{\lambda} \cos(h_s) \cos(\delta) + \frac{B_{NS}}{\lambda} \sin(h_s) \sin(lat) \cos(\delta) \quad (7)$$

We compare these nulls with known values of nulls for the Airy Disk function in equation 6. We focus our attention to the second half of the day, and estimate the nulls and thier associated error in terms of LST. We then use equation 7 to convert our estimates to a measure of projected baseline length in the east west direction.

We create a range of guesses for the angular ra-

dus θ_r and compute the predicted u values from the known nulls using the relation

$$u_{pred} = \frac{x_{known}}{2\pi\theta_r} \quad (8)$$

Where x_{known} are the table valued nulls of eq 6 and θ_r is the angular radius of the sun. We now define χ^2 as

$$\chi^2 = \sum_i \frac{|u_{pred} - u_i|^2}{\sigma_i^2} \quad (9)$$

and compute this for a range of θ_r 's. We the minimum value of this will represent the most likely value of θ_r and the 2σ error will be twice the minimum χ^2 value. Figure 5 shows the minima of this brute force χ^2 minimization technique and highlights the 2σ confidence level. We then fit an Airy Disk with the parameters for phase, and amplitude using our estimate of the angular radius, as well as for the 2σ

above and below estimates to check if our envelope works with our data.

Figure 6 show our fit of the modulating function along with these errors, as well as our data, all as a function of u . We see that the fit for the data matches fairly well at the smaller u values and begins to fail towards the larger projected baselines.

In this calculation we are using so few points to actually compute the χ^2 . A more accurate approach to this could be fitting an Airy disk to our data and performing a chi squared analysis on the fit. We save this for future work.

We find that the most likely value of the angular radius of the sun occurs at $.259^{+0.011^\circ}_{-0.010^\circ}$. As a check we use this value of θ_r , along with the upper and lower bounds of the 2σ errors, and compute eq 6 with the argument $x = 2\pi u\theta_r$ for the second half of 2458924 *JD*.

5 Discussion

With our estimated angular radius of the sun, we can use the known distance to the sun 1 *AU*, and calculate the actual solar radius, which is just the $1 \text{ AU} \cdot \sin \theta_r$. We find the actual radius to be $6.763 \times 10^{8+2.872 \times 10^7 m}_{-2.611 \times 10^7 m}$.

We compare this with the most recent estimates of the suns radius and find that they are $6.96156 \times 10^8 \pm 1.45 \times 10^6 m$. Which is a value on the higher end of our 2σ error bar. We still find that there is considerable accuracy in our measurements and χ^2 analysis with only 4 data points.

The modulating function becomes important when we consider the visibility equation,

$$V(u, v) = e^{-2\pi i w} \int A(l, m) I(l, m) e^{-2\pi i (ul + vm)} dl dm \quad (10)$$

Where $A(l, m)$ is a function representing the beam, $I(l, m)$ is the source intensity, and l, m are coordinates describing the source location on the sky. The first term is the point source fringe rate and represents the rate at which the source is moving through the projected fringe pattern on the sky, the second term is a representation of the modulating function of the source its self.

6 Conclusion

In this work, we used a radio interferometer to calculate the precise location of the interferometer baseline, and used this to perform a χ^2 analysis on our

data, estimating the angular radius of the sun. We verified that our estimates and errors were within the range of the most recent observations of the solar radius, and considered what this means in terms of the visibility and modulating function.

We provide strong evidence for the sun as a disk on the sky based off of its Fourier transform being strongly modeled by an Airy Disk which we see in the data. With that being said, there is also evidence that the sun cannot be modelled as a perfect disk. This can be seen in the fact that towards 0 *LST*, we find that the modelled Airy Disk falls fails to fully encapsulate the data as seen by the data falling far out of the 2σ range. Further, there seems to be a stretching of the function at noon, breaking the expected symmetry that would exist if the sun was a perfect disk.

While we were able to make an accurate measurement of the sun, we are in the process of performing a more detailed estimate by performing a χ^2 minimization on not just four points, but on a fully extracted enveloping function. This would provide a much higher accuracy estimate because of the number of points involved, and reduce the length of our error bars. Preliminary work has begun on this project.

7 Acknowledgements

For this project, Connor, James, and Basil worked together to develop the code, I performed most of the observations, we worked together on the analysis.

References

Event Horizon Telescope Collaboration. First M87 Event Horizon Telescope Results. I. The Shadow of the Supermassive Black Hole. , 875(1):L1, April 2019. doi: 10.3847/2041-8213/ab0ec7.